npj | heritage science

Article

https://doi.org/10.1038/s40494-025-01646-6

Application of a Full-Field macro-XRF imaging spectrometer to non-invasive investigation of elemental composition in three-dimensional artworks

Check for updates

Bartłomiej Łach[1] ✉, Tomasz Fiutowski[1], Julio M. del Hoyo-Meléndez[2], Stefan Koperny[1], Paulina Krupska-Wolas[1,2], Bartosz Mindur[1], Piotr Wiącek[1], Paweł M. Wróbel[1] & Władysław Dąbrowski[1]

This article explores the performance and capabilities of a custom-developed full-field XRF imaging spectrometer operating at limited energy resolution (1.1 keV FWHM at 5.9 keV) for elemental mapping of three-dimensional (3D) objects. The measurements performed involved two, different in spatial depth, historical artworks from the collection of the National Museum in Krakow. The first is an object of low significance, used in principle as a phantom, while the second is an actual cultural heritage object. The resulting maps of elemental distributions are presented, along with detailed descriptions and a discussion on pigment identification. Finally, specific features, analysis artefacts, as well as benefits and limitations of the system are discussed. The results obtained for the investigated objects confirm the capability of the developed instrument for XRF elemental imaging of 3D objects and its usefulness in the field of cultural heritage research.

Today, Macro X-Ray Fluorescence (MA-XRF), as one of the possible variants of the XRF technique, is a well-established research method, especially among the heritage science community. Mapping of chemical elements distributions in the surface layers of artwork helps art historians and conservators, for example, to identify the inorganic pigments found in cultural heritage (CH) objects[1], to verify the quality of conservation treatments carried out in the past[2,3], or to support investigations dealing with the provenance or authenticity of CH objects[4,5]. Hidden internal layers with preparatory drawings or original sketches can also be revealed[6,7]. Given the multi-spectral capabilities and non-invasive character of the MA-XRF technique, it is also suitable for applications in other fields such as biology, geology, or forensics[8–12]. Although there are a few commercially available spectrometers[13–15], numerous custom-designed instruments have been developed by different scientific groups and laboratories[16–19].

As most MA-XRF spectrometers are designed to scan objects using focused X-ray micro-beams, their use is generally limited to the investigation of flat objects. If the investigated surface is not located precisely in the focal plane of the micro-beam, the beam risks to aim at a point different from the one aimed from the detector. Although investigations of objects with moderate surface curvature can be performed successfully[20,21], measurements of objects with non-flat surfaces will result in significant degradation of spatial resolution and visible blurring of the obtained elemental maps[22]. Moreover, in the case of complex 3D objects the shadowing effect is unavoidable, i.e. some fraction of excited X-ray radiation may not reach the detector, because of absorption in fragments of the object on the way from the excitation point to the detector resulting in significant reduction of signals or even completely blocked signals from some parts of the investigated object.

Significant improvements have been made recently to address the issues mentioned above. For example, non-uniform sensitivity can be worked around by a proper data correction procedure[23] and a new method for reconstructing the topography of the object[24] has been proposed. In turn, the shadowing effect can be mitigated by applying two detectors mounted in opposite directions[19]. Some solutions have also been proposed to solve the problem of spatial resolution degradation with varying detector-object distance, such as an innovative Aperture Management System (AMS) from Bruker Nano GmbH[25] or automatic detector-object distance adjustment systems, in which the measurement head follows the surface curvature of the investigated object[19,26,27]. Another interesting solution for proper positioning, although developed for Particle-Induced X-ray Emission (PIXE)[28], can be suitable for MA-XRF spectrometers. The use of a cable-robot-based positioning system, as an alternative to the typical stacked linear motorised stages, is also worth noting[29].

[1]AGH University of Krakow, Faculty of Physics and Applied Computer Science, al. A. Mickiewicza 30, 30-059 Krakow, Poland. [2]Laboratory of Analysis and Non-Destructive Investigation of Heritage Objects, The National Museum in Krakow, al. 3 Maja 1, 30-062 Krakow, Poland. ✉e-mail: bartlomiej.lach@fis.agh.edu.pl

Despite all the improvements mentioned above, the use of scanning MA-XRF instruments for investigating 3D CH objects remains a challenging task. Taking into account the typical working distance between the investigated object and the detector in such spectrometers (~1.0 cm), measurements of most 3D objects with considerably irregular shapes may turn out to be a really hard task. The safety of the investigated objects when a measurement head moves close to them is another concern. Therefore, in addition to standard scanning systems, one may consider an alternative approach based on Full-Field X-Ray Fluorescence (FF-XRF) imaging[30–33]. Such systems allow for measurements with a larger distance between the instrument head and the object, resulting in safer movement of the instrument around valuable objects. Moreover, the application of pinhole camera optics, which in principle has infinite depth of field, enables measurements of 3D objects without compromising the spatial resolution of the spectrometer. Some examples of imaging results can be found in refs. 34–37. However, the investigated objects are rather reliefs and not full 3D shapes. Other solutions worth noting for elemental imaging of non-flat objects are also those based on photogrammetric modelling combined with point XRF analysis[38,39] or computer tomography combined with full-field imaging[40].

In this paper, we present the capabilities of a custom-developed FF-XRF imaging spectrometer for applications involving 3D types CH objects. To improve the data analysis process, machine learning algorithms such as Non-negative Matrix Factorisation (NMF) have been implemented to complement the traditional Region of Interest (ROI) method.

Experimental

MA-XRF spectrometer

The MA-XRF imaging results presented in the paper were obtained using a custom-developed FF-XRF spectrometer. A sketch of the spectrometer concept is shown in Fig. 1.

A detailed description of the system can be found elsewhere[41]. In short, the instrument consists of two X-ray tubes (Varian VF-50J 50W @ 1 mA and 50 kV operation) with pinhole camera optics[42], a position-sensitive and energy-dispersive detector with an active area of 10 cm × 10 cm based on Gas Electron Multiplier (GEM) technology, a custom-design detector readout system based on Application Specific Integrated Circuits (ASICs) and a controller based on Field-Programmable Gate Array (FPGA) technology[43]. All components are mounted in a box with dimensions 88 cm × 30 cm × 17 cm and weight of approximately 10.0 kg, which is attached to the robotic arm.

The GEM detector used in the described spectrometer is a gaseous type detector working in the proportional regime. Briefly, it is a micro-pattern gaseous detector consisting of drift electrode followed by three successive GEM foils and a readout structure enclosed in a not perfectly tight chamber flushed with a gas mixture based on one of noble gases. The detector working principle is based on the ionisation of gas atoms followed by the multiplication of the generated electrons in GEM foils and finally collection of the generated electron clouds on readout electrodes using a properly formed electric field. Although the development of GEM detectors is primarily driven by their applications in high energy physics experiments, they are also suitable for simultaneous spectral and position-sensitive measurements of low-energy X-rays, up to about 20 keV.

Applied GEM detector is equipped with a 2D strip-like Cartesian readout structure with a readout pitch of 0.8 mm resulting in a spatial resolution σ_s of 110 µm[44]. The energy resolution averaged over all the sensitive area of the detector is typically 1.1 keV Full Width at Half Maximum (FWHM) at 5.9 keV. The quantum efficiency varies strongly with X-ray energy and for argon-based gas mixture is about 32% for 4 keV going down to 3.1% for 10 keV. These parameters are determined by the operating principle of gaseous detectors and fundamental physical phenomena[45]. The energy resolution and especially quantum detection efficiency are relatively low, compared to silicon 0D detectors, which offer energy resolution at a level of 150 eV FWHM at 5.9 keV with detection efficiency of about 99% (450 µm absorption depth). Nevertheless the GEM detectors like the one that we have used are still useable for our application. It is worth noting that to the best of our knowledge, the energy resolution of our detector is one of the best reported in the literature for GEM detectors[46–49]. It has been achieved by using an advanced readout system and calibration procedures.

The images of the measurement head and the ready-to-use system with the measurement head mounted on the robotic arm are shown in Fig. 2. Using six degrees of freedom of the robotic arm, proper alignment of the measurement head and the examined object can easily be ensured.

Although the spectrometer can operate in different optic configurations, i.e. with different optical magnification, in the reported measurements the following set of parameters was used: (a) optical magnifications of ×1, (b) investigation area of 10 cm × 10 cm, (c) 65 mm length pinhole camera with two different diameters (1 and 2 mm). Therefore, according to the formula

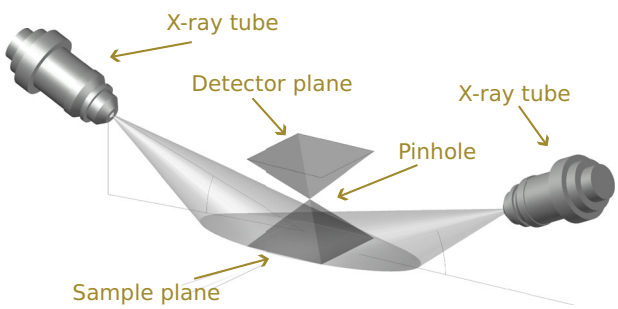

Fig. 1 | Schematic diagram of the working principle of the system with two X-ray tubes and a pinhole camera.

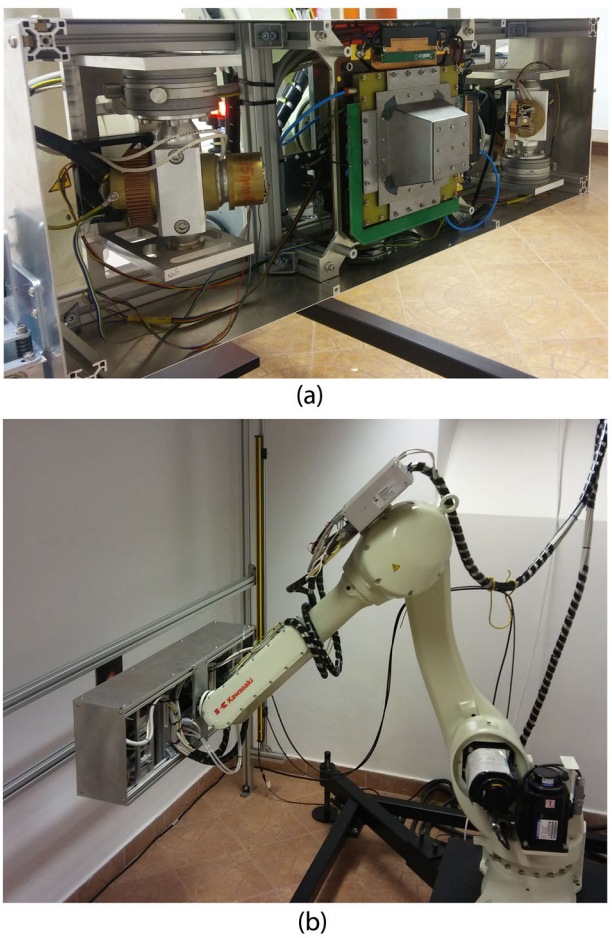

Fig. 2 | Image of the FF-XRF spectrometer developed within this project. Measurement head (**a**) mounted on the robotic arm (**b**).

Fig. 3 | Images of the investigated low-significance object *Fragment of ornament from a church altar*. Front-side (**a**), half-profile (**b**), profile (**c**).

Fig. 4 | Images of the four different sides of *Inkwell with lid*.

Table 1 | Measurement settings

Object	No. of frames	Acquisition time for one frame [min]	Measured area [cm²]
Fragment of ornament from a church altar	4	20	20 × 18
Inkwell with lid	4[a]	32	8 × 6

[a]Each one of the four sides of the object was measured in a single frame.

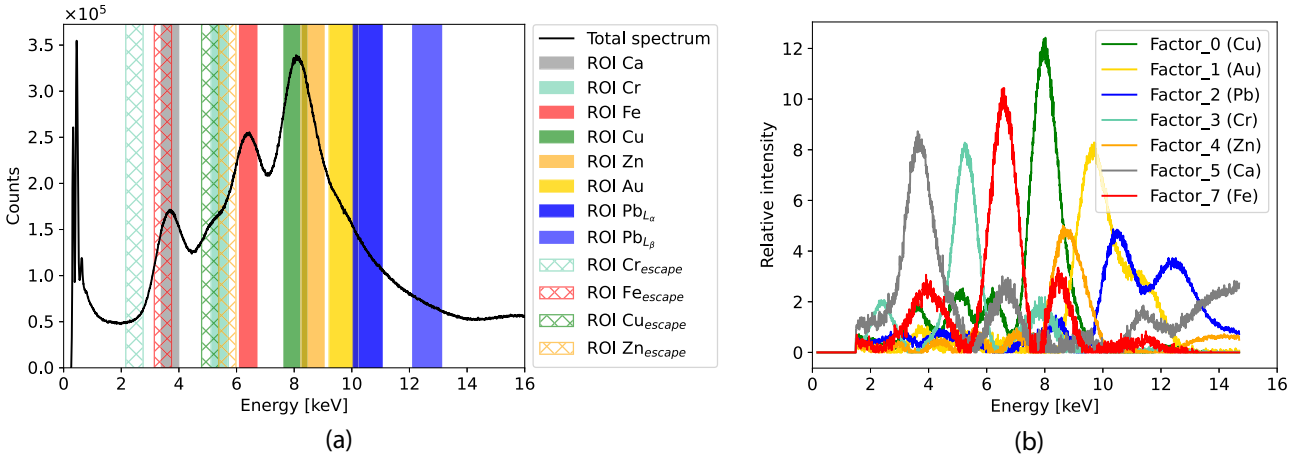

Fig. 5 | Results obtained for *Fragment of ornament from a church altar*. Cumulative spectrum for the whole measured area with marked 12 ROIs (**a**); factor composition obtained from NMF analysis (**b**).

presented in ref. 50, the resulting spatial resolution in the central part of the detector was 0.9 and 1.7 mm (rms) for 1 and 2 mm, respectively.

Investigated objects

Two different CH objects were investigated: a low-significance object and an actual CH object. From the point of view of the developed measurement technique, this represents a different range of spatial depth (the distance between the closest and farthest part of the object seen by the detector), which allows to evaluate the performance of the system over a wide depth of field. In addition, for one of the investigated objects we have tested the stitching procedure of adjacent frames, which for objects with highly irregular shapes can be a challenge due to the operating principle of the pinhole camera and the geometry of the measurement system.

The first investigated object is a gilded wooden fragment of the ornament of a Rococo altar from the church of St. Mary Magdalene located in Dukla (city in the Podkarpackie province, Poland). Images of the object are shown in Fig. 3 showing three profiles. It would fit into a box with dimensions 20 cm × 18 cm × 3 cm.

For this study, modifications were made to the object to enhance its elemental composition complexity. Five different reference commercial paints were applied to the surface of the object. Minium (red lead) was used for the orange areas, viridian and malachite (chrome and copper greens, respectively) were used for the green parts, and cadmium yellow was used for the vertical yellow stripe in the lower, central portion of the object. Furthermore, a narrow horizontal section at the base of the object was coated with a layer of silver.

The second object *Inkwell with lid* shown in Fig. 4 is an example of artistic craftsmanship. The object is dated to the second half of the sixteenth century and was made using techniques such as forging, gilding, and engraving. The inkwell in the form of a cylinder is decorated on the entire surface with four ancient scenes (The Judgment of Paris, Apollo and Marsyas, The Astronomer, and a scene with Satyr and Satyress), separated by herms. A lid with a pinnacle ending in a ball is decorated with festoons, masks, and shields. Its dimensions are 8 cm in height and 6 cm in diameter.

Measurement procedure

The developed spectrometer is based on a GEM detector, which requires a specific preparatory procedure to deal with effects like non-uniformity of the gas amplification factor across the active area or charging up effects resulting in drifts of gas amplification factor in time and its dependence on the local count rates across the detector area. A detailed description can be found in ref. 41, here only the major steps are mentioned: (1) detector high voltage bias applied for at least 10 h before the planned measurement, (2) measurement of the XRF radiation from a pure copper calibration plate, (3) placement of the object in the holder and adjustment of the measurement head with respect to the object plane, (4) selection of the investigation area and calculation of the measurement frames, (5) illumination of the first frame for 15 min before collecting any data, (6) scanning the object frame by frame according to a predefined route (automatic procedure). The movement and positioning plan of the measurement head is carried out using the robot control panel according to the embedded dedicated software.

The key measurement settings for all the investigated objects are summarised in Table 1.

Methodology of data analysis

To handle all analysis tasks and provide relatively easy data treatment, a custom-developed software based on the Python programming language using the *NumPy* package for scientific computing has been implemented[51,52]. After initial data pre-processing, that is, data merging, application of all necessary correction, calibration procedures, etc., the final data set in the form of a compressed *numpy* array (two axes correspond to the X and Y coordinates of the pixel and the third to its energy spectrum) was created. The overall procedures of data analysis are described in ref. 41.

After the data were processed, the final elemental distribution maps were generated. For both investigated objects listed in Table 1, two different methods were applied: (1) ROI analysis, and (2) NMF. For generation of the ROI maps, individual ROIs were manually selected using the cumulative energy spectrum constructed using the data from the entire investigated area of the given object. The maps from NMF analysis were derived using algorithms implemented in the *hyperspy* library[53].

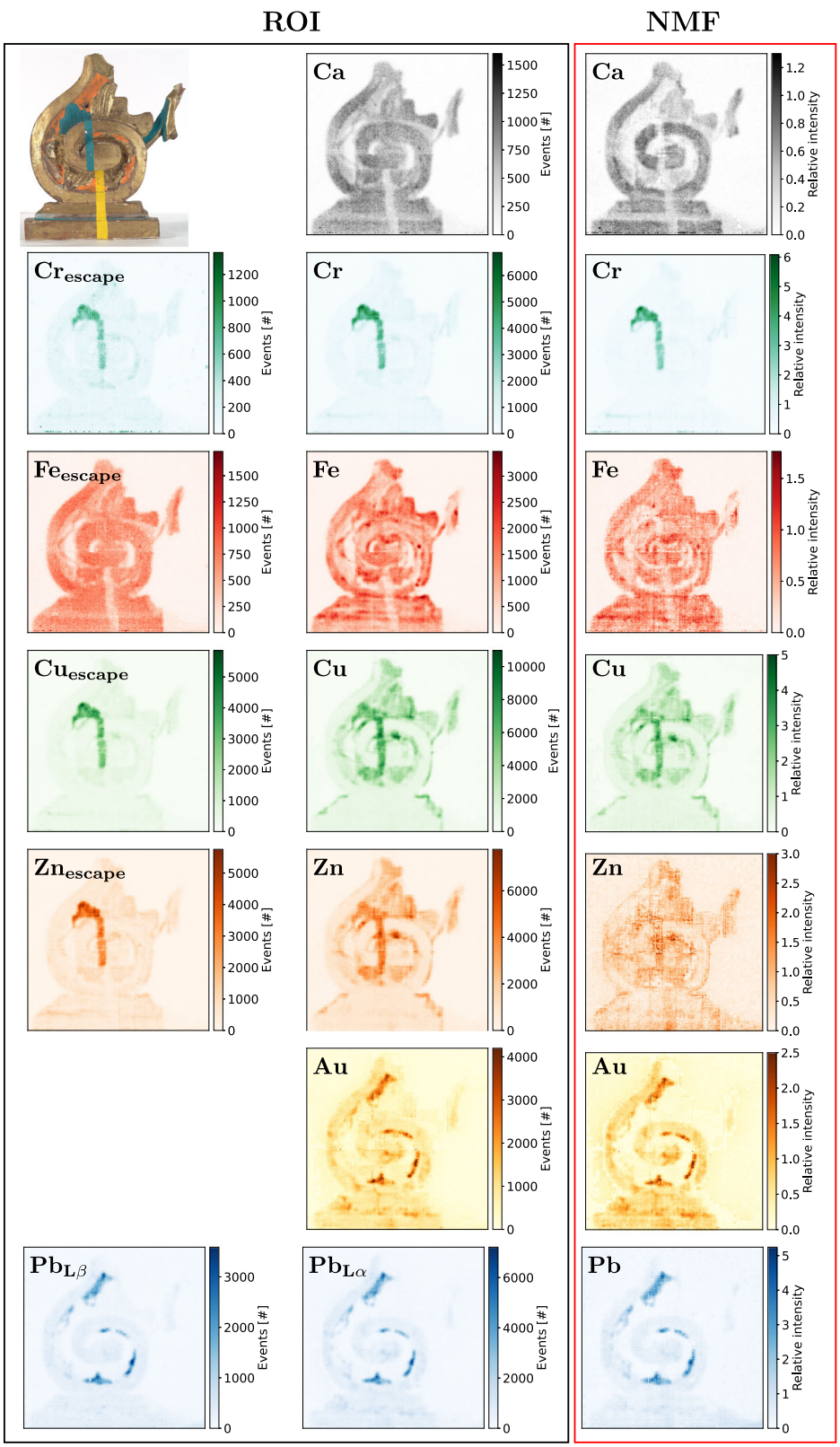

Fig. 6 | Elemental distribution maps obtained for the *Fragment of ornament from a church altar* by two different analysis methods: ROI (first two columns) and NMF (third column).

Selection of the above methods results mainly from our previous work[41], in which we evaluated and compared in details performances, advantages, and limitations of standard ROI method and NMF factorisation algorithm. Briefly, while the ROI method works perfectly in the case of well-separated characteristic peaks of individual elements, it fails completely for spectra with low-energy resolution. The NMF analysis provided significant enhancement in selectivity of the elemental analysis, including detection of elements completely invisible in the cumulative spectra.

In general, the NMF algorithm performs decomposition of the input data matrix using an orthogonal transformation into two smaller sets: the eigenvectors (basis vectors) and the loadings, which describe how much each data point contributes to a particular component. Due to the constraint of the

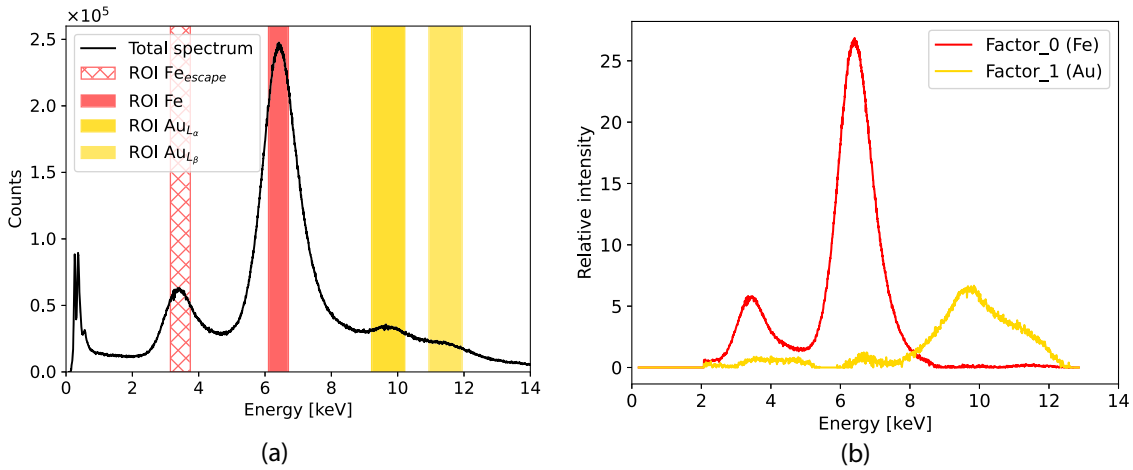

Fig. 7 | Results for the object *Inkwell with lid*. Cumulative spectrum for the whole measured area with marked four ROIs (**a**); factor composition obtained from the NMF analysis (**b**).

factorisation results to non-negative values only, individual components fully reflect the nature of XRF data, which allows for their relatively simple identification. Therefore the NMF algorithm is very widely used tool that supports the analysis of spectroscopic data of cultural heritage. In particular, it allows for the separation of overlapping XRF spectra of two different elements. However, it should be noted that factor representation cannot be interpreted quantitatively in terms of the concentration of elements in the investigated objects. In case of data obtained from our spectrometer, individual basis vectors can be interpreted as XRF spectrum of single elements, while individual loadings as distribution maps of these elements.

When discussing the results presented, it should be noted that the energy resolution of the GEM detector is limited, as mentioned before. Another specific feature of the GEM is the appearance of a satellite energy peak in the energy spectrum associated with each characteristic energy line. This escape peak corresponds to the characteristic energy lowered by 2.95 keV in the case of the argon-based gas mixture employed, which in turn corresponds to the characteristic energy of argon. Therefore, combining the two above mentioned methods helps to resolve some ambiguities which may occur during the interpretation of the data.

Results and discussion

Fragment of ornament from a church altar

The results obtained for the object are shown in Figs. 5 and 6. Figure 5a shows the total cumulative spectrum collected from the entire investigated area with the selected ROIs. Due to the high complexity of the spectrum and the limited energy resolution, the assignment of only a few energy peaks with the corresponding energy line is straightforward (copper, iron, and calcium K_α lines). All additional ROIs were added in the second iteration, after observations of the results obtained from the NMF analysis. Although the wide and long tail of the spectrum may suggest the potential occurrence of elements with higher fluorescence energies, their identification and selection of specific ROI ranges based only on the spectrum cannot be justified. Each such attempt should be considered essentially as a 'blind' search.

Figure 5b shows the composition of the factors obtained from the NMF analysis. The NMF reveals seven quite easily distinguishable factors, which can be assigned to the following set of elements: calcium, chromium, iron, copper, zinc, gold, and lead. The comparison of maps of loadings obtained from NMF analysis and the intensity maps for all ROIs marked in Fig. 5a spectra is shown in Fig. 6. Some particular observations can be formulated based on the maps obtained.

Despite irregular shapes of the object, the stitching procedure of the adjacent frames (object measured in four individual frames) is working correctly. No significant artefacts or discontinuities between the combined areas can be seen on the maps obtained.

The observed spatial resolution of the system remains constant and completely independent of the depth at which a given fragment of the investigated area is located at the object's surface. This conclusion is confirmed by visual inspection of the horizontal insertion painted using chrome green paint. Despite a 2 cm difference in depth at which fragments of insertions are placed, the observed spatial resolution at each position is identical, i.e., the sharpness of edges remains the same along the insertion.

The chromium, zinc, gold, and lead signals detected by the NMF method are in agreement with the ROI maps, which clearly confirm the presence of these elements in the investigated object. The zinc and gold elemental distributions require an additional comment. Unlike the ROI technique, the NMF method indicates a complete absence of zinc in the area covered with chrome green paint, as expected. As already mentioned, during the preparatory process, the considered area, in addition to the chrome green paint, was additionally covered with a layer of copper-rich malachite. Hence, it is not surprising (due to the close proximity of the copper and zinc K_α lines and the limited energy resolution of the system) that it appears on the zinc ROI map. Therefore, the map obtained by the NMF method is considered correct. In the case of gold distribution, both the ROI and the NMF techniques provide virtually identical, consistent maps. However, both contain a dominant lead signal. Due to the relatively close proximity of the L_α lines of both elements (difference of approximately 0.84 keV), this effect is expected for the ROI method. In contrast, in the case of the NMF method, a better separation of these two signals could be expected. However, because of the large number of elements present in the data set and limited statistics, separation is limited.

The ROI maps corresponding to escape peaks of copper and zinc are virtually the same as the ROI map of chromium. This is not surprising, as the energies of all three considered signals are located in very close proximity. Since the chromium signal has a much higher intensity than the others, it dominates the maps of both escape peaks. This particular case proves the advantage of the NMF method. On the map of copper distribution, the signal from chromium is much weaker, and on the map of zinc it is hardly noticeable.

The spatial distributions of iron and calcium obtained using the ROI and NMF methods are consistent with each other. However, it should be noted that for calcium, the NMF version has higher selectivity (contrast). Similarly to the previously described chromium case, the significantly higher intensity of the calcium signal in relation to the signal of the iron escape peak results in the ROI map of the latter does not differ from the ROI map for calcium. Here, it is worth noting the area of reduced intensity, which corresponds to the location of the painted yellow stripe observed in the distributions of both considered elements. In addition, a vertical stripe of reduced intensity is also visible in the upper part of the calcium NMF map.

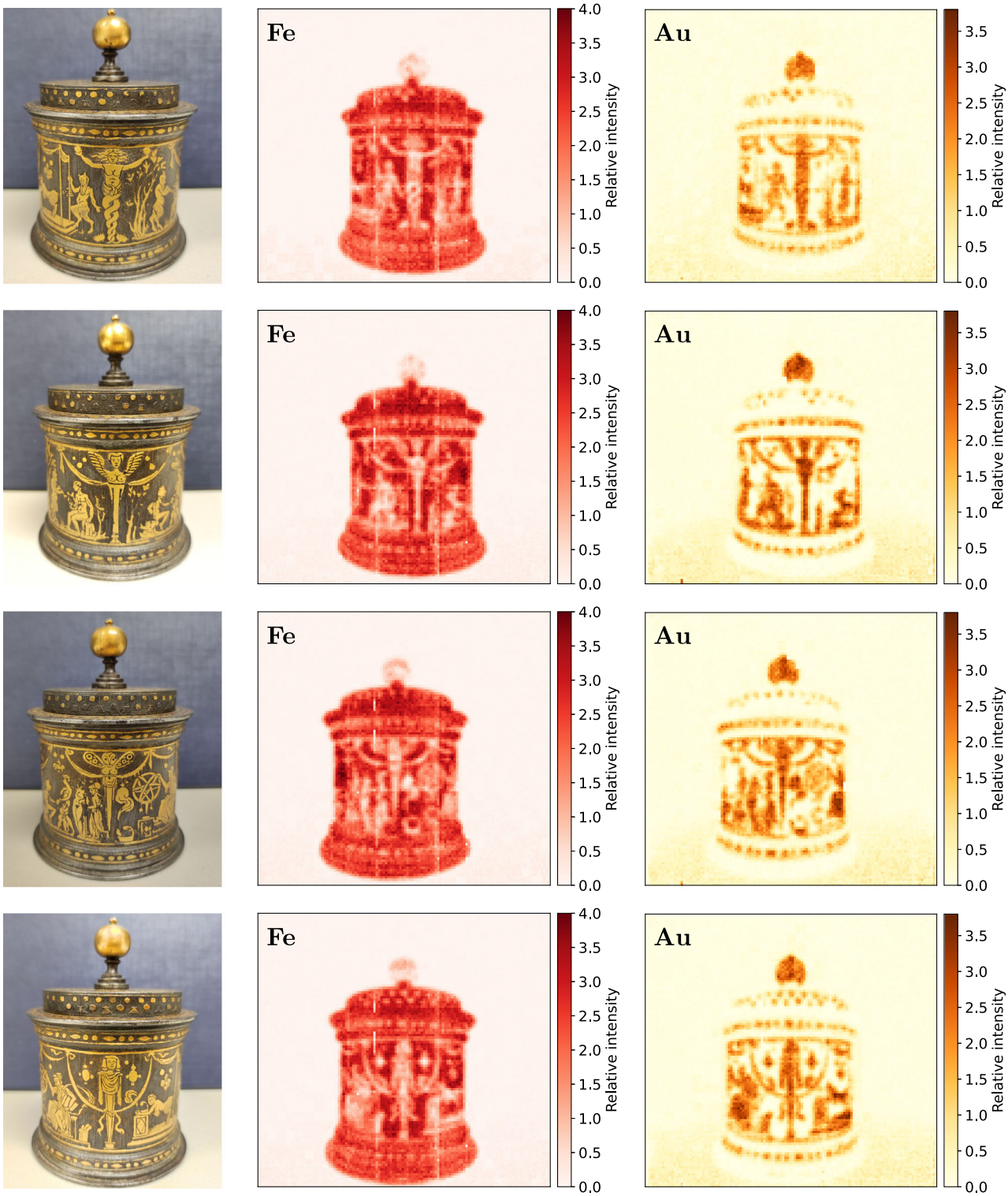

Fig. 8 | Elemental distribution maps obtained for the *Inkwell with lid* using the NMF analysis method.

This area corresponds to the location of the chrome-green painted inserts. This is due to the absorption of low-energy X-ray photons from calcium and iron in the overlaying stripe.

Although the signal related to the yellow vertical stripe was not detected directly by any of the applied analysis techniques, valuable information was revealed in the calcium and iron maps. That is, the element that creates this pigment must have a high absorption capacity. By combining this information with the other results obtained, it is possible to identify the considered yellow pigment using the deduction technique. Since the yellow strip is not represented by lead, zinc, iron, chromium, or calcium maps, it excludes the following set of pigments: naples yellow, lead-tin yellow, massicot, zinc yellow, chromium yellow, lemon yellow, yellow ochre, and Indian yellow. As a result, the filtration carried out above leaves only four potential candidates: orpiment (king's yellow), cobalt yellow, bismuth-vanadate yellow, and cadmium yellow. If an arsenic-rich orpiment was used, its signal would certainly be observed on the lead map (fluorescence energy line of $As_{K_\alpha} \approx Pb_{L_\alpha}$). A similar situation occurs for cobalt and bismuth-vanadate pigments, for which the base elements have fluorescence lines

located in close proximity to the iron, lead, and chromium energy lines, respectively. In the case of cobalt yellow, its signal would be visible on the iron distribution map, while for bismuth-vanadate yellow on the lead and chromium maps. Because none of the described situations is observed, the conclusion is to reject the three considered candidates and to associate the yellow strip with the only remaining pigment, that is, cadmium yellow. This is in agreement with the knowledge possessed a priori and proofs that despite the lack of direct detection of a given element and moderate system energy resolution, pigment identification using some indirect solutions is still possible.

Similarly to the cadmium yellow pigment discussed above, the silver signal was also not detected. Because of the anode material of the X-ray lamps (molybdenum), both silver and cadmium are identified in the fluorescence spectrum by the L-line only. Because emission efficiency of L-lines of silver and cadmium are relatively low (about seven times lower compared to the L-line of lead), their contributions to such a complex spectrum is virtually negligible. However, the presence of these elements is indicated by absorption of excited low-energy X-rays, in particular, of calcium characteristic X-rays.

The analysis of the *Fragment of ornament from a church altar* described in the above section demonstrates the capabilities of the system and shows the complexity of the entire data analysis process. For the next object under investigation, although both techniques were applied, only the analysis results of the best-performing method are presented.

Inkwell with lid

Figure 7 shows the cumulative XRF spectrum and the compositions of factors received by the NMF method for the investigated CH object *Inkwell with lid*. Although four different sides of the object were measured, no differences were observed for the cumulative spectrum and the factors obtained. Thus, Fig. 7 only shows the results for one selected measurement frame.

The investigation carried out resulted in the detection of iron and gold elements. The elemental distribution maps obtained for each of the four different measurement frames are shown in Fig. 8. The iron signal is observed over the entire area of the examined object, except for the fragments corresponding to the gold decorations. The distribution obtained is expected and fully understood, as regions of decreased iron intensity correspond to the outer gold layer, which attenuates the signal from iron. The detected element should only be identified with the construction material of the inkwell, not with the pigment. As mentioned above, the recorded signal of gold corresponds to the golden decorations depicting ancient scenes, festoons, masks, and the ball located at the top of the lid. Therefore, the reconstructed elemental distributions fully confirm the use of gold as a decorative material.

The *Inkwell with lid* object, due to its cylindrical shape, is suitable for quantitative studies related to the infinite depth of field of the pinhole camera. The performance of our system regarding the expected infinite depth of field can be assessed by calculating the Laplacian of different parts of the image using the *The OpenCV Library* and *Laplacian()* function[54]. Here, the idea of using the Laplacian algorithm is to find areas of rapid changes in each part of the image, and then calculate the variance for the parts considered based on the Laplacian output in a similar way to that presented in ref. 55. We have divided the image of each four sides of the object into five vertical slices as shown in Fig. 9.

These areas were chosen to investigate the effect of increasing the distance between the camera and a given slice—see Fig. 4. The Laplacian operator (which is effectively an edge detection algorithm) is applied to each fragment. Following edge detection, the variance is calculated to measure the amount of details in each slice. Due to the nature of the variance, no specific threshold value can be attributed to out-of-focus images. However, the higher its value, the greater the number of detectable details in the image. Although the actual values of variance do not provide a direct measure of the depth of field, they can be used to compare the fragments. For infinite depth of field, the variance of the Laplacian should be similar for all fragments,

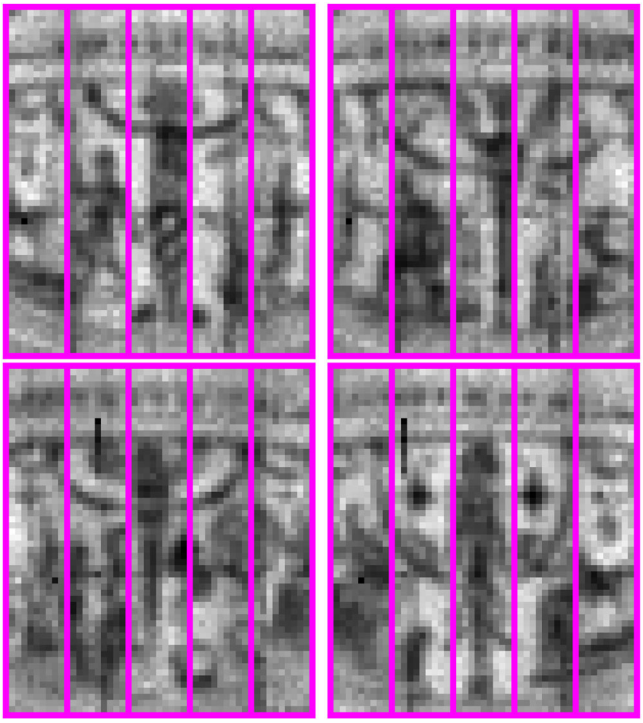

Fig. 9 | Original XRF images of each side (iron maps) of the central part of the *Inkwell with lid* object, with marked fragments used for variance estimation (see also Table 2).

Table 2 | Values of averaged (over four sides) and normalised variance for the captured XRF image fragments shown in Fig. 9; the higher variance value the more details in the given fragment

Slice no.	Variance
1	1.12
2	1.14
3	0.82
4	0.96
5	0.97

provided that the compositions of different fragments comprise a similar number and distribution of details. In addition, we normalised the variance values using overall average from all four object sides to ease of comparison.

The results are shown in Table 2. There are no significant differences between the fragments, which indicates that the depth of field is not affected by the variable distance between the object and the pinhole camera. This confirms the large depth of field of the developed system and its ability to image 3D objects.

Conclusions

This work presents the capabilities and performance of the developed XRF full-field imaging spectrometer applied to elemental mapping of 3D objects. The pinhole camera optics offer in principle infinite depth of field of the imaging system and indeed this feature has been clearly demonstrated in two case studies involving 3D objects.

Measurements and data analysis were performed on two different objects: a wooden fragment of a Rococo altar ornament and a decorated inkwell with cylindrical form. In both objects, the depth of the imaged areas varies up to 3 cm and no noticeable decrease in spatial resolution was observed. Such a range of focal depth is beyond the reach of MA-XRF spectrometers that use a focused X-ray microbeam.

It should be noted that the imaging results presented in the paper were obtained for a fixed geometry of the investigated object and the spectrometer head. Therefore, no manipulation of the object and/or the instrument is required during a given measurement session. In the case of valuable historical objects, this feature is greatly appreciated by art historians and conservators.

Data availability

The data presented in this study are available on request from the corresponding author.

Abbreviations

AMS	Aperture Management System
ASIC	Application Specific Integrated Circuit
CH	Cultural heritage
FF	Full-Field
FF-XRF	Full-Field X-Ray Fluorescence
FPGA	Field-Programmable Gate Array
FWHM	Full Width at Half Maximum
GEM	Gas Electron Multiplier
MA-XRF	Macro X-Ray Fluorescence
NMF	Non-negative Matrix Factorisation
PIXE	Particle-Induced X-ray Emission
ROI	Region of Interest
XRF	X-Ray Fluorescence

Received: 13 September 2024; Accepted: 24 January 2025;
Published online: 03 March 2025

References

1. Van Loon, A. et al. Artificial orpiment, a new pigment in Rembrandt's palette. *Herit. Sci.* **5**, 26 (2017).
2. Van der Snickt, G. et al. In situ macro X-ray fluorescence (MA-XRF) scanning as a non-invasive tool to probe for subsurface modifications in paintings by P.P. Rubens. *Microchem. J.* **138**, 238–245 (2018).
3. Gerodimos, T. et al. Scanning X-ray fluorescence data analysis for the identification of Byzantine icon's materials, techniques, and state of preservation: a case study. *J. Imaging* **8**, https://www.mdpi.com/2313-433X/8/5/147 (2022).
4. Saverwyns, S., Currie, C. & Lamas-Delgado, E. Macro X-ray fluorescence scanning (MA-XRF) as tool in the authentication of paintings. *Microchem. J.* **137**, 139–147 (2018).
5. Harth, A., Van der Snickt, G., Schalm, O., Janssens, K. & Blanckaert, G. The young Van Dyck's fingerprint : a technical approach to assess the authenticity of a disputed painting. *Herit. Sci.* **5**, 13 (2017).
6. Pessanha, S., Costa, M., Sampaio, J. M. & Carvalho, M. L. Revealing the hidden preliminary version of Eça de Queiroz "The Illustrious House of Ramires" using X-ray micro-analysis. *Nucl. Instrum. Methods Phys. Res. Sect. B Beam Interact. Mater. At.* **371**, 396–400 (2016).
7. Favero, P. A. et al. Reflectance imaging spectroscopy and synchrotron radiation X-ray fluorescence mapping used in a technical study of The Blue Room by Pablo Picasso. *Herit. Sci.* **5**, 26 (2017).
8. Leppänen, J. J., Saarinen, T., Jilbert, T. & Oulasvirta, P. The analysis of freshwater pearl mussel shells using μ-XRF (micro-x-ray fluorescence) and the applicability for environmental reconstruction. *SN Appl. Sci.* **3**, https://doi.org/10.1007/s42452-020-03978-3 (2021).
9. Chen, Y., Li, X., Ten, F., Chen, J. & Reisz, R. R. Micro-XRF mapping study on the taphonomy of a Jurassic larval salamander fossil from inner Mongolia of China. *At. Spectrosc.* **44**, 24–31 (2023).
10. Flude, S., Haschke, M. & Storey, M. Application of benchtop micro-XRF to geological materials. *Mineral. Mag.* **81**, 923–948 (2017).
11. Geil, E. C., LeBlanc, S. A., Dale, D. S. & Thorne, R. E. Application of X-ray fluorescence imaging to ceramics from the American Southwest. *J. Archaeol. Sci.* **40**, 4780–4784 (2013).
12. Knijnenberg, A., van Loon, A., Dik, J. & van Asten, A. Elemental imaging of forensic traces with macro- and micro-XRF. In *Leading Edge Techniques in Forensic Trace Evidence Analysis* (ed. Blackledge, R. D.) Ch. 7, 213–244 (John Wiley & Sons, Ltd, 2022).
13. Bruker Nano GmbH, M4 TORNADO Plus. https://www.bruker.com/products/x-ray-diffraction-and-elemental-analysis/micro-xrf-and-txrf/m4-tornado-plus/overview.html. Accessed 17 June 2024.
14. Bruker Nano GmbH, M6 Jetstream. https://www.bruker.com/products/x-ray-diffraction-and-elemental-analysis/micro-xrf-and-txrf/m6-jetstream/overview.html. Accessed 17 June 2024.
15. IXRF Systems, Atlas. https://www.ixrfsystems.com/atlas_m/. Accessed 17 June 2024.
16. Figueroa, R. G. et al. Characteristics of a robust and portable large area X-ray fluorescence imaging system. *X-Ray Spectrom.* **43**, 126–130 (2014).
17. Ravaud, E. et al. Development of a versatile XRF scanner for the elemental imaging of paintworks. *Appl. Phys. A Mater. Sci. Process.* **122**, 17 (2016).
18. Ruberto, C. et al. Imaging study of Raffaello's "La Muta" by a portable XRF spectrometer. *Microchem. J.* **126**, 63–69 (2016).
19. Romano, F. P. et al. Real-time elemental imaging of large dimension paintings with a novel mobile macro X-ray fluorescence (MA-XRF) scanning technique. *J. Anal. At. Spectrom.* **32**, 773–781 (2017).
20. Vanden Berghe, I., Van Bos, M., Vandorpe, M. & Coudray, A. Non-invasive analysis of heritage textiles with MA-XRF mapping—exploring the possibilities. The study of Bishop Jacques de Vitry's mitres and fragile medieval reliquary purses from Namur (Belgium). *Herit. Sci.* **11**, https://doi.org/10.1186/s40494-023-00977-6 (2023).
21. Cavaleri, T. et al. Below the surface of the coffin lid of Neskhonsuennekhy in the Museo Egizio collection. *X-Ray Spectrom.* **50**, 279–292 (2021).
22. Bruker Nano GmbH. New horizons of micro-XRF in art and conservation. The art and conservation webinar series—part I. https://www.bruker.com/en/news-and-events/webinars/2020/new-horizons-of-micro-xrf-in-art-and-conservation.html. Accessed 17 June 2024.
23. Alfeld, M., Gonzalez, V. & Van Loon, A. Data intrinsic correction for working distance variations in MA-XRF of historical paintings based on the Ar signal. *X-Ray Spectrom.* **50**, 351–357 (2021).
24. Ippoliti, M., Billè, F., Karydas, A. G., Gianoncelli, A. & Kourousias, G. Reconstruction of 3D topographic landscape in soft X-ray fluorescence microscopy through an inverse X-ray-tracing approach based on multiple detectors. *Sci. Rep.* **12**, 20145 (2022).
25. Bruker Nano GmbH, AMS system. https://www.bruker.com/en/products-and-solutions/elemental-analyzers/micro-xrf-spectrometers/m6-jetstream/the-aperture-management-system-ams-.html. Accessed 17 June 2024.
26. Szalóki, I., Gerényi, A. & Radócz, G. Confocal macro X-ray fluorescence spectrometer on commercial 3D printer. *X-Ray Spectrom.* **46**, 497–506 (2017).
27. Wang, W., Shu, L. & Wang, D. Soft body reconstruction of a reptile fossil by the nondestructive elemental mapping with a newly designed XRF. *Isl. Arc* **32**, e12495 (2023).
28. Calligaro, T. et al. A new 3D positioner for the analytical mapping of non-flat objects under accelerator beams. *Nucl. Instrum. Methods Phys. Res. Sect. B Beam Interact. Mater. At.* **467**, 65–72 (2020).
29. Alfeld, M., Tempel, P. & Van der Wijk, V. Cable robots as conventional linear stage alternatives for the investigation of complex-shaped objects via macroscopic X-ray fluorescence imaging. *Quantum Beam Sci.* **7**, https://www.mdpi.com/2412-382X/7/4/37 (2023).
30. Dąbrowski, W. et al. Application of GEM-based detectors in full-field XRF imaging. *J. Instrum.* **11**, C12025–C12025 (2016).
31. Bjeoumikhov, A. et al. The SLcam: a full-field energy dispersive X-ray camera. *J. Instrum.* **7**, C11008–C11008 (2012).

32. Romano, F. P. et al. Macro and micro full field X-ray fluorescence with an X-ray pinhole camera presenting high energy and high spatial resolution. *Anal. Chem.* **86**, 10892–10899 (2014).
33. Walter, P. et al. Full-field XRF instrument for cultural heritage: application to the study of a Caillebotte painting. *X-Ray Spectrom.* **48**, 274–281 (2019).
34. De Samber, B. et al. Three-dimensional X-ray fluorescence imaging modes for biological specimens using a full-field energy dispersive CCD camera. *J. Anal. At. Spectrom.* **34**, 2083–2093 (2019).
35. An, S., Krapohl, D., Norlin, B. & Thungström, G. Full-field X-ray fluorescence imaging with a straight polycapillary X-ray collimator. *J. Instrum.* **15**, P12033 (2020).
36. Carvalho, P. M. S. et al. Elemental mapping of Portuguese ceramic pieces with a full-field XRF scanner based on a 2D-THCOBRA detector. *Eur. Phys. J. Plus* **136**, https://doi.org/10.1140/epjp/s13360-021-01422-y (2021).
37. Leite, F. D. et al. Analysis of Zebrafish contamination with heavy metals using a FF-XRF imaging system based on a MPGD. *Spectrochim. Acta Part B At. Spectrosc.* **198**, 106545 (2022).
38. Alfeld, M. et al. The Eye of the Medusa: XRF imaging reveals unknown traces of antique polychromy. *Anal. Chem.* **89**, 1493–1500 (2017).
39. Emmitt, J., McAlister, A., Bawden, N. & Armstrong, J. XRF and 3D modelling on a composite Etruscan helmet. *Appl. Sci.* **11**, https://www.mdpi.com/2076-3417/11/17/8026 (2021).
40. Vavrik, D., Kumpova, I., Vopalensky, M. & Zemlicka, J. Mapping of XRF data onto the surface of a tomographically reconstructed historical sculpture. *J. Instrum.* **14**, C02003 (2019).
41. Łach, B. et al. Application of factorisation methods to analysis of elemental distribution maps acquired with a full-field XRF imaging spectrometer. *Sensors* **21**, https://www.mdpi.com/1424-8220/21/23/7965 (2021).
42. Wróbel, P. M. et al. Modelling of vignetting effects in full-field X-ray fluorescence imaging system based on pinhole optics. *Spectrochim. Acta Part B At. Spectrosc.* **171**, 105934 (2020).
43. Fiutowski, T. et al. ARTROC—a readout ASIC for GEM-based full-field XRF imaging system. *J. Instrum.* **12**, C12016–C12016 (2017).
44. Fiutowski, T., Dąbrowski, W., Mindur, B., Wiącek, P. & Zielińska, A. Design and performance of the GEMROC ASIC for 2-D readout of gas electron multiplier detectors. In *2011 IEEE Nuclear Science Symposium Conference Record, Valencia*. 1540–1544 (2011).
45. Sipilä, H. Energy resolution of the proportional counter. *Nucl. Instrum. Methods* **133**, 251–252 (1976).
46. Malinowski, K. et al. Simulation of energy spectrum of GEM detector from an X-ray quantum. *J. Instrum.* **13**, C01018 (2018).
47. Roy, S. et al. Stability study of gain and energy resolution for GEM detector. *Nucl. Instrum. Methods Phys. Res. Sect. A Accel. Spectrom. Detect. Assoc. Equip.* **936**, 485–487 (2019).
48. Phan, N. S., Lee, E. R. & Loomba, D. Imaging 55Fe electron tracks in a GEM-based TPC using a CCD readout. *J. Instrum.* **15**, P05012 (2020).
49. Velásquez Moros, A. & Castro Serrato, H. F. Characterization and calibration of a triple-GEM detector for medical dosimetry. *Nucl. Instrum. Methods Phys. Res. Sect. A Accel. Spectrom. Detect. Assoc. Equip.* **1000**, 165241 (2021).
50. Silva, A. L. M. et al. Characterization of an energy dispersive X-ray fluorescence imaging system based on a Micropattern Gaseous Detector. *Spectrochim. Acta Part B At. Spectrosc.* **66**, 308–313 (2011).
51. Python Software Foundation, Python Language Reference. http://www.python.org. Accessed 17 June 2024.
52. Numpy-fundamental package for scientific computing with Python. http://www.numpy.org. Accessed 17 June 2024.
53. Hyperspy-generic multi-dimensional data analysis toolbox. https://hyperspy.org/. Accessed 17 June 2024.
54. Bradski, G. The OpenCV Library. *Dr. Dobb's Journal of Software Tools* (2000).
55. Pech Pacheco, J. L., Cristobal, G., Chamorro-Martinez, J. & Fernandez-Valdivia, J. Diatom autofocusing in brightfield microscopy: a comparative study. In *Proceedings 15th International Conference on Pattern Recognition. ICPR-20003*, **3**, 314–317 (2000).

Acknowledgements

B.Łach. has been partly supported by the EU Project POWR.03.02.00-00-I004/16. This work was partially supported by the Polish National Centre for Research and Development, grant no. PBS3/A9/29/2015.

Author contributions

Conceptualisation: B.M., T.F., P.M.W., and W.D.; methodology: B.M., T.F., J.H.-M., and P.M.W.; software: B.Ł., B.M., and P.K.-W.; validation: B.Ł., T.F., and W.D.; formal analysis: B.Ł. and T.F.; investigation: B.Ł. and P.K.-W.; resources: B.M., T.F., S.K., and P.W.; data curation: B.Ł.; writing—original draft preparation: B.Ł.; writing—review and editing: B.Ł., T.F., B.M., J.H.-M., and W.D.; visualisation: B.Ł.; supervision: W.D.; project administration: W.D.; funding acquisition: W.D. All authors read and agreed to the published version of the manuscript.

Competing interests

The authors declare that they have no competing interests. The funders had no role in the design of the study; in the collection, analysis or interpretation of data; in the writing of the manuscript; or in the decision to publish the results.

Additional information

Correspondence and requests for materials should be addressed to Bartłomiej Łach.